Energy & Environmental Science

ROYAL SOCIETY OF CHEMISTRY

PAPER

View Article Online
View Journal | View Issue

Cite this: *Energy Environ. Sci.*, 2025, **18**, 9478

High-entropy-induced CoO_6 octahedral distortion for boosted oxygen evolution reaction at high temperature

Geng Zou,†[ab] Hewei Liu,†[ac] Tianfu Liu,†[a] Shaobo Han,[a] Zijian Tan,[ab] Shaowei Zhang,[a] Yige Guo,[ab] Jingcheng Yu,[ab] Xiaomin Zhang,[a] Fang Lu,[a] Yuefeng Song,*[a] Guoxiong Wang*[ad] and Xinhe Bao[a]

Modulation of the distortion of BO_6 octahedra plays a pivotal role in determining the physicochemical properties and electrocatalytic performance of the perovskite oxides ($ABO_{3-\delta}$). By tailoring the degree of octahedral tilting and bond angle, the electronic structure, oxygen vacancy, and ionic transport pathways within the perovskite lattice could be finely tuned. Herein, we propose an efficient strategy to tune the BO_6 (CoO_6) octahedral distortion through A-site high-entropy engineering in the $Nd_{0.2}Pr_{0.2}La_{0.2}Ba_{0.2}Sr_{0.2}CoO_{3-\delta}$ anode, with the average Co–O–Co angle decreasing from 175° to 149°. *Ex situ* and *in situ* characterization studies combined with density functional theory calculations reveal that the high-entropy-induced CoO_6 octahedral distortion shifts the O 2p band center of the perovskite anode towards the Fermi level, thereby activating the lattice oxygen and accelerating the transport of oxygen ions. Electrochemically, the CoO_6-distorted $Nd_{0.2}Pr_{0.2}La_{0.2}Ba_{0.2}Sr_{0.2}CoO_{3-\delta}$ anode delivers enhanced high-temperature oxygen evolution reaction (OER) performance in solid oxide electrolysis cells (SOECs), achieving a high current density of 3.96 A cm^{-2} at 800 °C and 1.5 V along with excellent stability over 600 hours, which is superior to that of most reported anode materials. This work discloses the impact of CoO_6 octahedral distortion on high-temperature OER performance at the atomic scale and proposes an effective strategy for designing efficient and durable anodes of SOECs.

Received 9th March 2025,
Accepted 24th September 2025

DOI: 10.1039/d5ee01370d

rsc.li/ees

Broader context

Solid oxide electrolysis cells (SOECs) offer a highly efficient pathway for converting CO_2 into chemicals and fuels using clean energy sources. However, their performance is often limited by the sluggish kinetics of the oxygen evolution reaction (OER) at the anode. High-entropy perovskites (HEPs) have garnered attention as promising candidates for addressing this challenge due to their tunable electronic structures and unique physicochemical properties. However, the structure–activity relationship governing their high-temperature OER performance remains poorly understood. This study investigates the role of A-site high entropy in modulating B-site CoO_6 octahedral distortion and strain, which are key factors influencing lattice oxygen activity and OER kinetics. *Via* electrochemical characterization, and *in situ* physicochemical, and density functional theory calculations, we reveal that entropy-driven CoO_6 octahedral distortion enhances lattice oxygen activity, significantly improving OER performance. These insights provide a fundamental understanding of high-entropy effects in SOEC anodes and offer a rational strategy for designing efficient and durable electrode materials, with broad implications for materials science, catalysis, and energy conversion.

1. Introduction

Solid oxide electrolysis cells (SOECs) are highly efficient energy conversion devices capable of utilizing clean, primary energy sources such as solar, wind, and geothermal to convert CO_2 into chemical fuels. This process can effectively reduce greenhouse gas emissions and store electricity generated by intermittent renewable energy sources.[1–3] During CO_2 electrolysis in SOECs, CO_2 is reduced to CO and O^{2-} at the cathode (eqn (1)), and then the O^{2-} ions migrate through the electrolyte to the anode,

[a] *State Key Laboratory of Catalysis, Dalian National Laboratory for Clean Energy, Dalian Institute of Chemical Physics, Chinese Academy of Sciences, Dalian, 116023, Liaoning, China. E-mail: songyf2014@dicp.ac.cn, wanggx@dicp.ac.cn*
[b] *University of Chinese Academy of Sciences, Beijing, 100039, China*
[c] *College of Light Industry and Chemical Engineering, Dalian Polytechnic University, Dalian, 116034, China*
[d] *Department of Chemistry, Advanced Institute of Future Energy, Shanghai Key Laboratory of Electrochemical and Thermochemical Conversion for Resources Recycling, iChEM (Collaborative Innovation Center of Chemistry for Energy Materials), Fudan University, Shanghai, 200438, China*
† These authors contributed equally to this work.

where the oxygen evolution reaction (OER) occurs, generating O_2 (eqn (2)).[4,5] The OER involves a four-electron transfer process, consuming a substantial amount of electrical energy. Additionally, its sluggish kinetics limit the electrochemical performance of SOECs.[6,7] Therefore, developing efficient anode materials is crucial for SOEC technology.

$$CO_2 + 2e^- \rightarrow CO + O^{2-} \quad (1)$$

$$2O^{2-} \rightarrow O_2 + 4e^- \quad (2)$$

Perovskite oxides are commonly used as SOEC anodes due to their high mixed ionic and electronic conductivity (MIEC), compatible thermal expansion coefficient with electrolyte, relatively high OER activity, and excellent thermal stability.[4,5] Extensive research on developing advanced anodes has focused on tuning the lattice oxygen activity of perovskite oxides by customizing ion ordering,[8] optimizing the electronic structures,[9] introducing oxygen non-stoichiometry,[10,11] and fabricating dislocation-segmented subgrains.[12] Recently, high-entropy perovskites (HEPs) have been widely used in solid oxide cells, solar cells, lithium ion batteries and other energy fields, owing to their rich elemental composition, tunable electronic structure, and unique physicochemical properties caused by high configurational entropy.[13,14] In HEPs, the high configurational entropy is defined by eqn (S1),[13,15,16] where A and B denote the number of element types on the A-site cation and B-site cation, respectively. The symbols x_a, x_b, and x_j represent the molar fractions of the corresponding elements, and R is the gas constant. Typically, five or more metal elements in molar ratios of 5%–35% and $\Delta S_{config} \geq 1.5R$ are considered as the main characteristics for HEPs.[13,17]

The cocktail effect, lattice distortion, and hysteretic diffusion effect in HEP electrodes contribute to enhanced catalytic activity, accelerated reaction kinetics, and mitigated performance degradation caused by cation segregation or grain growth.[18–23] For instance, Liu *et al.* synthesized $Pr_{1/6}La_{1/6}Nd_{1/6}Ba_{1/6}Sr_{1/6}Ca_{1/6}CoO_{3-\delta}$ (PLNBSCC) as an oxygen electrode in reversible protonic ceramic electrochemical cells, which achieved a current density of 1.95 A cm^{-2} at 1.3 V and 600 °C, along with 200 hours stability attributed to the improved MIEC of the PLNBSCC electrode.[21] He *et al.* applied A-site entropy engineering to develop $Pr_{0.2}Ba_{0.2}Sr_{0.2}La_{0.2}Ca_{0.2}CoO_{3-\delta}$ as a reversible solid oxide cell air electrode, which exhibited decreased polarization resistance (R_p) due to its good chemical compatibility with the electrolyte, increased ion diffusivity and oxygen exchange rates.[22] However, the structure–activity relationship of HEPs for high-temperature OER in the SOECs has been rarely investigated, especially the impact of high-entropy engineering on the distortion of CoO_6 octahedra, which is closely related to the lattice oxygen activity and OER performance.

Herein, based on $La_{0.6}Sr_{0.4}CoO_3$ (LSC, ΔS_{config} = 0.67R), we designed and synthesized an A-site high-entropy $Nd_{0.2}Pr_{0.2}La_{0.2}Ba_{0.2}Sr_{0.2}CoO_{3-\delta}$ (NPLBSC, ΔS_{config} = 1.61R) by strategically introducing rare earth elements Nd, Pr and alkaline earth element Ba at the A-site. X-ray diffraction (XRD) and high-angle annular dark field-scanning transmission electron microscopy (HAADF-STEM) confirmed the atomic-scale microstructure changes. X-ray photoelectron spectroscopy (XPS), X-ray absorption spectroscopy (XAS), O_2 temperature-programmed desorption (O_2-TPD), $^{18}O_2$ isotope exchange, electrical conductivity relaxation (ECR), *in situ* Raman spectroscopy, and density functional theory (DFT) calculations demonstrated that lattice oxygen activity of NPLBSC was improved due to the high-entropy-induced CoO_6 octahedral distortion. Finally, the NPLBSC anode delivered an ultra-high current density of 3.96 A cm^{-2} at 1.5 V and 800 °C, along with 600 hours stability, which is superior to LSC. This study establishes the relationship between CoO_6 octahedral distortion and high-temperature OER performance, providing a promising strategy for the design of active and stable anode materials for SOECs.

2. Results and discussion

2.1 Crystalline structure

The crystalline structures of LSC (Fig. 1a) and NPLBSC (Fig. 1d) were characterized *via* XRD, and both exhibit a cubic perovskite structure (space group $Pm\bar{3}m$).[24] The lattice parameters are $a = b = c$ = 3.8363 Å for LSC and 3.8400 Å for NPLBSC, respectively, indicating slight lattice expansion due to A-site high-entropy engineering. A slight shift of the diffraction peaks toward lower angles is observed in NPLBSC (Fig. S1), demonstrating an expansion of the lattice volume, which is further proved by the enlarged lattice spacings of NPLBSC compared to that of LSC in the HAADF-STEM images (Fig. 1b and e). *In situ* XRD patterns show (Fig. S2) that as the temperature increases from room temperature to 800 °C, the diffraction peaks of both samples shift slightly to lower angles due to lattice expansion, without the formation of secondary phases. This indicates that LSC and NPLBSC retain stable crystalline structures. Furthermore, the ε_{xx} strain maps obtained through geometric phase analysis (GPA) (Fig. 1c and f) reveal distinct differences in strain distribution. Obviously, the NPLBSC in Fig. 1f exhibits more pronounced tensile strain compared to LSC in Fig. 1c. Such lattice tensile strain can significantly promote the formation of oxygen vacancies, thereby enhancing OER activity at high temperatures.[25,26] Furthermore, the atomically resolved elemental maps of LSC (Fig. 1g) reveal that La and Sr are distributed at the A site, while Co is distributed at the B site. For NPLBSC (Fig. 1h), Nd, Pr, La, Ba, and Sr are uniformly distributed at the A site, while Co is uniformly distributed at the B site. In addition, larger-scale elemental maps of LSC (Fig. S3) and NPLBSC (Fig. S4) further confirm the uniform distribution of elements in the selected nanoparticles without cation aggregation.

To investigate the chemical bonding at the atomic scale, oxygen-atom-sensitive annular bright-field (ABF) imaging was employed to investigate lattice distortion of CoO_6 octahedra in LSC and NPLBSC along the [110] zone axis. As depicted in Fig. 2a and c, O atoms located between the adjacent Co atoms can be clearly observed in LSC and NPLBSC. Atomic positions were determined by locating the mass centers of each Co and O atom, followed by Gaussian fitting to measure the Co–O–Co angles for the samples (Fig. 2b and d). In LSC (Fig. 2b), nearly

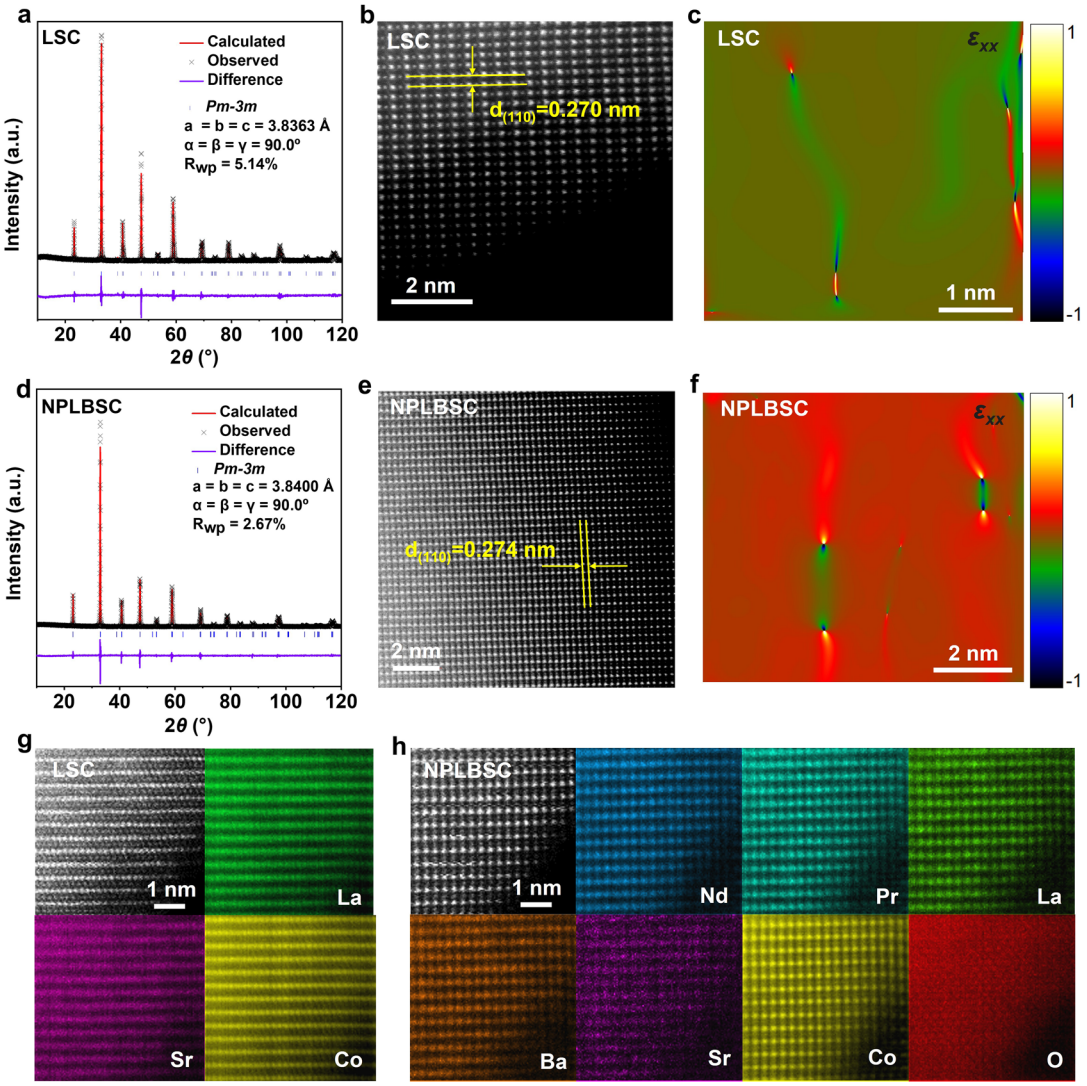

Fig. 1 Structural characterization. Refined XRD patterns of (a) LSC and (d) NPLBSC. HAADF-STEM image of (b) LSC and (e) NPLBSC. Geometric phase analysis (GPA) strain map of ε_{xx} of (c) LSC and (f) NPLBSC. HAADF-STEM elemental maps of (g) LSC and (h) NPLBSC.

all oxygen atoms are located at normal positions with an average Co–O–Co angle of 175°, indicating a minimal lattice distortion. In contrast, noticeable lattice distortion is observed in NPLBSC (Fig. 2d) with an average Co–O–Co angle of 149°, indicating a more pronounced distortion of the oxygen octahedra. This structural distortion is further supported by Raman spectra (Fig. S5), where a blue shift of Co–O stretching ($\sim$670 cm^{-1}) mode for NPLBSC compared to LSC.[27,28] The CoO_6 octahedral distortion is further quantified by the variation of Co–O bond lengths.[27,29] As shown in Fig. 2e, NPLBSC exhibits more pronounced Co–O bond length variation than LSC (Fig. 2f). To further explore the relationship between configurational entropy and lattice distortion, we synthesized $Pr_{0.3}La_{0.3}Sr_{0.4}CoO_{3-\delta}$ (PLSC) and $Nd_{0.2}Pr_{0.2}$ $La_{0.2}Sr_{0.4}CoO_{3-\delta}$ (NPLSC) samples and characterized their average Co–O–Co bond angles. The STEM-annular bright field (STEM-ABF) imaging results (Fig. 2a–d and Fig. S6) show that with the increase of configurational entropy, the Co–O–Co bond angle decreases, and the CoO_6 octahedral distortion degree (Δ) (Fig. 2g and Fig. S7) increases from 8.9×10^{-8} for LSC to 6.5×10^{-4} for NPLBSC. These results demonstrate that A-site entropy engineering leads to a more intricate lattice mismatch and strain distribution, causing evident distortion of the oxygen octahedra and altered coordination environment of the Co cations.

2.2 Electronic structures of transition metal

XPS was performed to investigate changes in the chemical state of transition metals in LSC and NPLBSC. Since the Ba 3d and Co 2p signals overlap in the XPS spectra, the oxidation state variation of Co was evaluated by the Co 3p XPS signal. As shown in Fig. 3a, the Co 3p XPS peak at $\sim$60.3 eV shifts slightly toward higher binding energy for NPLBSC, suggesting an increased average valence state of Co as a result of A-site entropy engineering.[8,30] XANES results (Fig. 3b and Fig. S8) show that Co K-edge of NPLBSC appears at the highest energy among the samples, indicating that Co in NPLBSC exhibits the highest

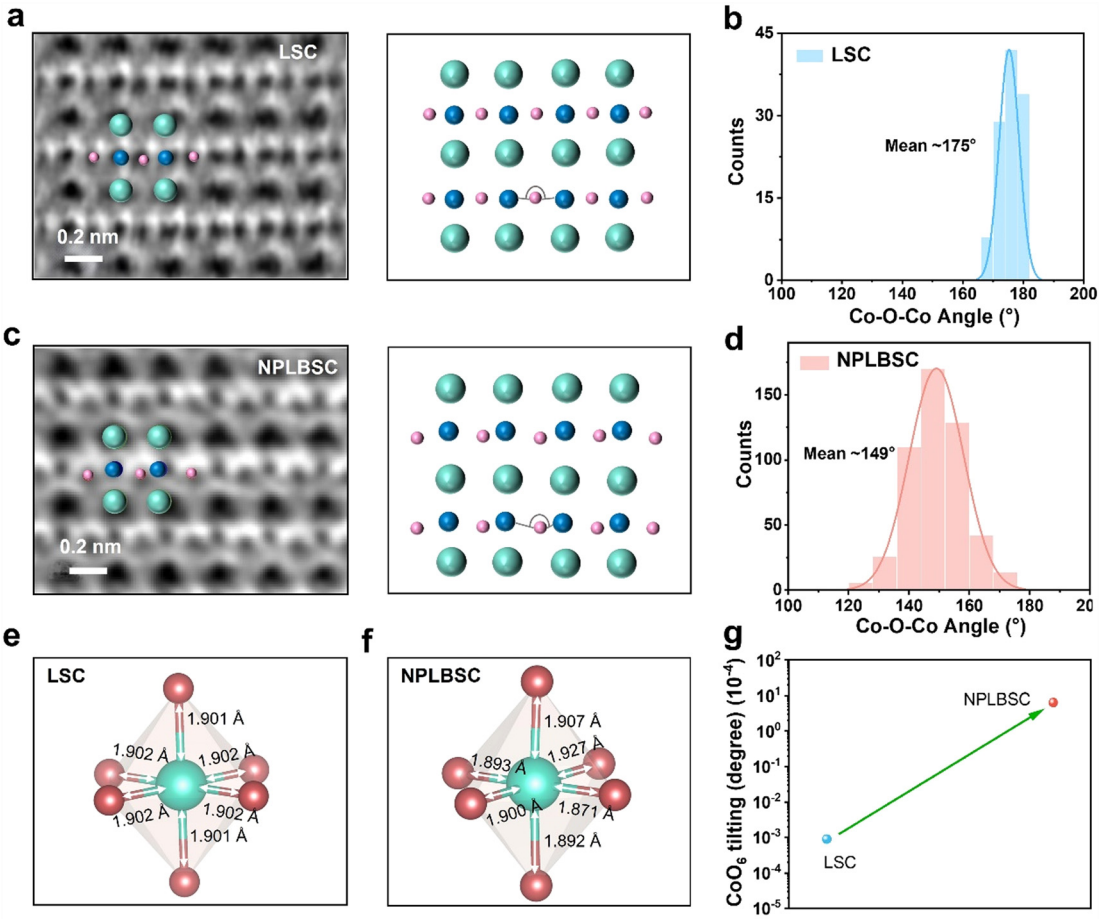

Fig. 2 STEM-ABF images of (a) LSC and (c) NPLBSC. Distribution of the Co–O–Co angle in (b) LSC and (d) NPLBSC. Bond structure in the CoO_6 octahedron in (e) LSC and (f) NPLBSC. (g) CoO_6 octahedral distortion degree (Δ) calculated by the equation $\Delta = \frac{1}{6}\sum\left(\frac{R_i - R_{av}}{R_{av}}\right)^2$ (where R_{av} is the average bond length, and R_i is the individual bond length of Co–O in the CoO_6 octahedron).

valence state. To further characterize the bulk Co valence state changes and the coordination geometry under SOEC operating conditions, *in situ* XAS measurements were performed using a custom-designed high-temperature setup. *In situ* XANES spectra (Fig. S9) show that the Co K-edge of both LSC and NPLBSC shifts toward lower energy as the temperature increases to 800 °C, indicating that the average valence states decrease. This reduction is attributed to the generation of more oxygen vacancies at high temperatures. Notably, the Co valence state in NPLBSC remains higher than that in LSC even at 800 °C. Additionally, the pre-edge of the Co K-edge XANES spectra for both LSC and NPLBSC exhibits no significant change with increasing temperature, indicating that the distortion of oxygen octahedra in both materials is only slightly affected by temperature.[31] Fig. 3c displays the Fourier transformed (FT) EXAFS spectra of LSC and NPLBSC. In both samples, three prominent peaks appear at around 1.5 Å, 3.0 Å, and 3.5 Å, corresponding to the Co–O, Co–O–A, and Co–O–Co bonds, respectively.[32,33] The EXAFS spectra (Fig. S10) and fitting results (Table S1) reveal that the Co–O bond length remains nearly constant, whereas the Co–O–A bond length decreases and the Co–O–Co bond length increases in NPLBSC. Moreover, both Co–O and Co–O–A bond lengths decrease as the temperature increases from room temperature to 800 °C. Additionally, the corresponding coordination numbers also decreases with rising temperature, suggesting a higher concentration of oxygen vacancies.[34] The wavelet transform (WT) of EXAFS spectra can perform multi-scale analysis in both R space and k space. The WT EXAFS spectra of LSC (Fig. 3d) and NPLBSC (Fig. 3e) show a maximum intensity at $k \sim 10$ Å^{-1}, which can be attributed to the Co–O–Co bond.[35] Notably, NPLBSC shows an increased intensity for Co–O–Co, indicating that the electronic environment has changed. Atomic-scale electron energy loss spectra (EELS) were also used to reveal the change of the Co valence state. The Co L_3/L_2 ratio is lower in NPLBSC compared to LSC (Fig. S11), indicating a higher Co valence state induced *via* A-site high-entropy engineering.[36] Moreover, an increased intensity of the peak at ~528 eV is observed (Fig. S12), and this peak corresponds to the excitation from the O 1s state to the hybridized O 2p–Co 3d state.[36,37] These results indicate that the CoO_6 octahedral distortion not only increases the Co valence state, but also strengthens the Co–O covalency, thereby promoting charge transfer between metal and oxygen atoms, which is beneficial for improving OER activity.[27,38,39]

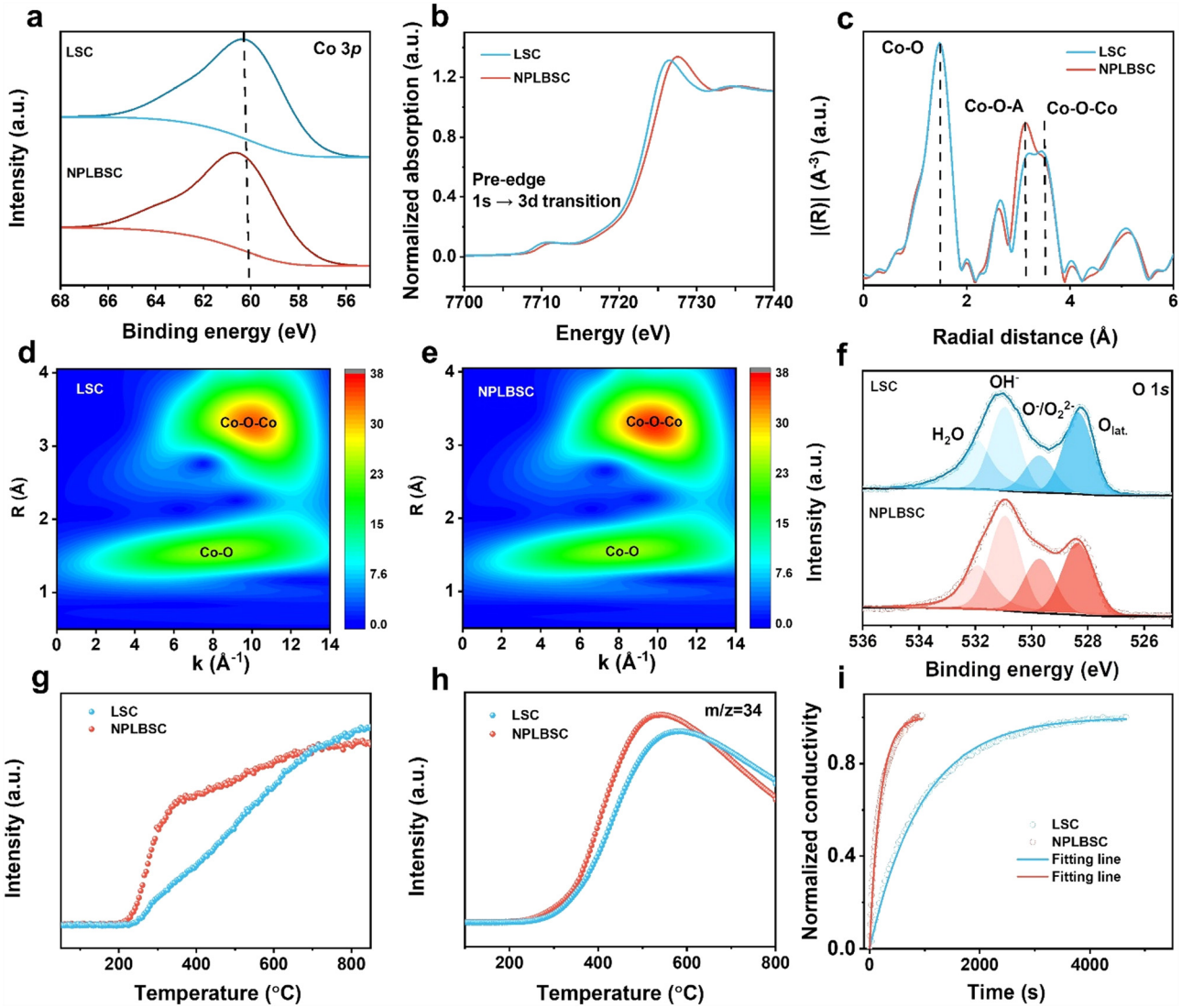

Fig. 3 Physicochemical properties of LSC and NPLBSC. (a) XPS spectra of Co 3p. (b) XANES at room temperature. (c) Extended X-ray absorption fine structure spectra (EXAFS) at room temperature. WT-EXAFS of (d) LSC and (e) NPLBSC at room temperature. (f) XPS spectra of O 1s. (g) O_2-TPD profiles. (h) Results of ^{18}O isotope exchange experiment. (i) ECR curves at 800 °C.

2.3 Lattice oxygen activity

XPS analysis of O 1s (Fig. 3f and Table S2) was conducted to investigate the effect of CoO_6 octahedral distortion on the surface oxygen properties. The amount of surface adsorbed oxygen species, including adsorbed O^- or O_2^{2-} species (~530.00 eV), adsorbed OH^- and carbonate (~531.00 eV), and adsorbed H_2O (~532.00 eV), increase from 70.27% in LSC to 74.43% in NPLBSC.[19] Electron paramagnetic resonance (EPR) measurements (Fig. S13) show that the unpaired electron signal at g = 2.003 for NPLBSC is evidently stronger than that for LSC, indicating higher oxygen vacancy concentration in NPLBSC. O_2 temperature-programmed desorption (O_2-TPD) profiles (Fig. 3g and Fig. S14) and thermogravimetric (TG) analysis (Fig. S15) reveal that NPLBSC shows the highest oxygen desorption peak intensity and greater weight loss compared to other samples. These results indicate that increasing the configurational entropy enhances the oxygen vacancy concentration, suggesting an improved oxygen vacancy formation capability in NPLBSC. The oxygen mobility of the samples was assessed by $^{18}O_2$ isotope exchange experiments. The signal of m/z = 34 represents $^{18}O^{16}O$ (g), originating from the exchange of the lattice oxygen with the $^{18}O_2$, and the peak area reflects the quantity of lattice oxygen involved in the oxygen exchange process.[8,9] As displayed in Fig. 3h, the peak area of NPLBSC is larger than that of LSC, indicating that more lattice oxygen in NPLBSC can participate in the oxygen exchange process, which further confirms that the lattice oxygen mobility of NPLBSC is higher than LSC. The surface oxygen exchange coefficient (k_{chem}) of LSC and NPLBSC were further investigated to study the effect of CoO_6 octahedral distortion on surface oxygen exchange capability. As presented in Fig. 3i, NPLBSC exhibits a higher k_{chem} (11.8×10^{-5} cm s^{-1}) than LSC (2.4×10^{-5} cm s^{-1}) at 800 °C, which suggests that the CoO_6 octahedral distortion in NPLBSC can enhance the surface oxygen exchange capability, potentially boosting the surface oxygen activity.

To gain further insight into the evolution of oxygen species during the OER in SOECs, *in situ* Raman spectroscopy was employed (Fig. 4a) to monitor the electrochemical spillover oxygen species on the anode surface under anodic polarization.[40–42] The *in situ* Raman spectra for LSC and NPLBSC anodes are shown in Fig. 4b and c, respectively. Clearly, with the application of various currents, oxygen species evolve on the surfaces of both LSC and NPLBSC. At the same time, with the increase of current from OCV to 100 mA, the peak intensity of –O–O$^-$ oxygen species becomes more obvious. However, the intensity of spillover oxygen species on NPLBSC is consistently higher than that on LSC under the same current, indicating that NPLBSC is more active for high-temperature OER than LSC.[40]

2.4 Density functional theory calculations

To investigate the effect of high-entropy engineering on the formation and evolution of oxygen vacancies in perovskites, we applied a random substitution at the A site of LSC perovskite to construct the NPLBSC models for DFT calculations, as shown in Fig. 5a. A total of 12 different configurations were analyzed based on their total energies to evaluate their stability. The most stable configuration, identified in Fig. 5b, exhibits the lowest energy (Fig. S16), suggesting it could be representative of a high-entropy perovskite model.

Furthermore, we calculated the formation energy of oxygen vacancy at different sites on surface and in bulk perovskite. The surface oxygen vacancy positions are shown in Fig. S17, and the bulk oxygen vacancy positions are shown in Fig. S18. As shown in Fig. 5c and d, the formation energies of oxygen vacancies on the surface and in bulk high-entropy perovskite are significantly reduced compared to the pristine LSC perovskite. Specifically, the surface oxygen vacancy formation energies at three different sites of NPLBSC are −0.54, −0.86, and −0.28 eV, which are lower than those of LSC (0.03, −0.6, and −0.13 eV) at the corresponding sites. And the bulk oxygen vacancy formation energies at three different sites of NPLBSC are 0.7, 0.35, and 0.14 eV, respectively, which are also lower than those of LSC (1.04, 1.94, and 0.98 eV) at the corresponding sites. The reduced formation energy indicates that the NPLBSC has more oxygen vacancies, which is consistent with results of O_2-TPD and TG, suggesting enhanced oxygen transport properties for the OER. We further investigated the electronic structure of LSC

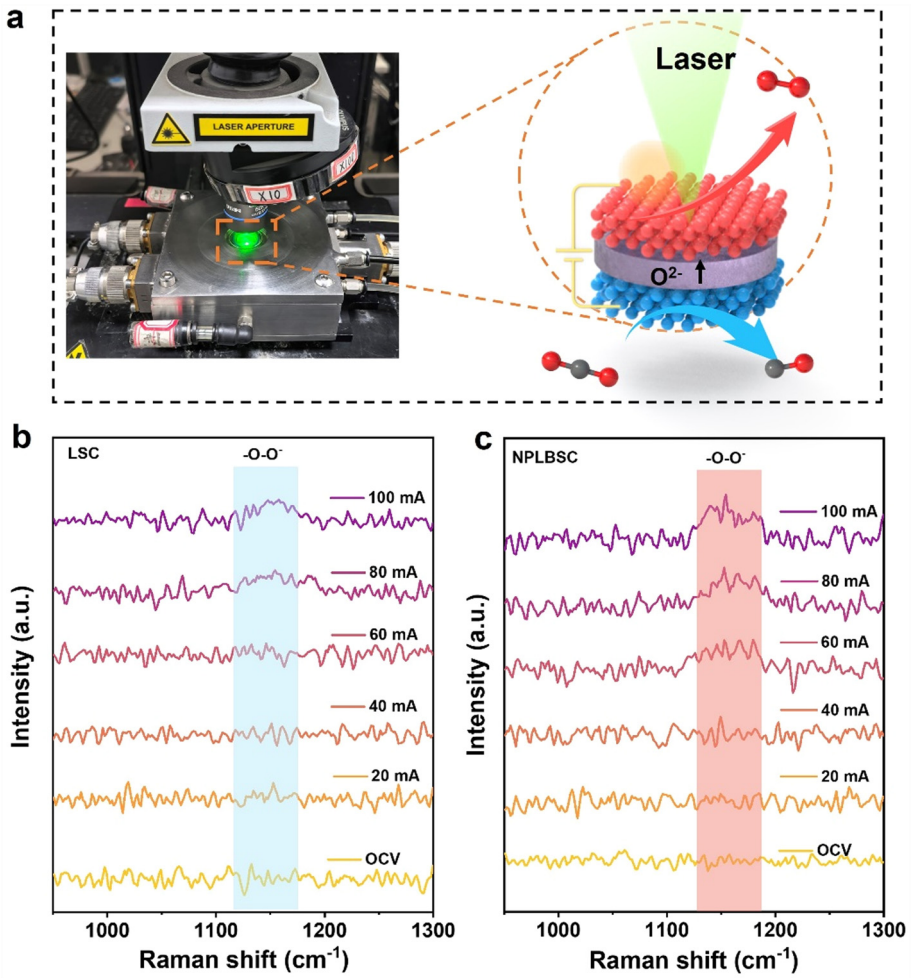

Fig. 4 *In situ* Raman spectroscopy tests. (a) Picture and schematics of the *in situ* Raman spectroscopy cells. *In situ* Raman spectra of (b) LSC and (c) NPLBSC at 600 °C, respectively.

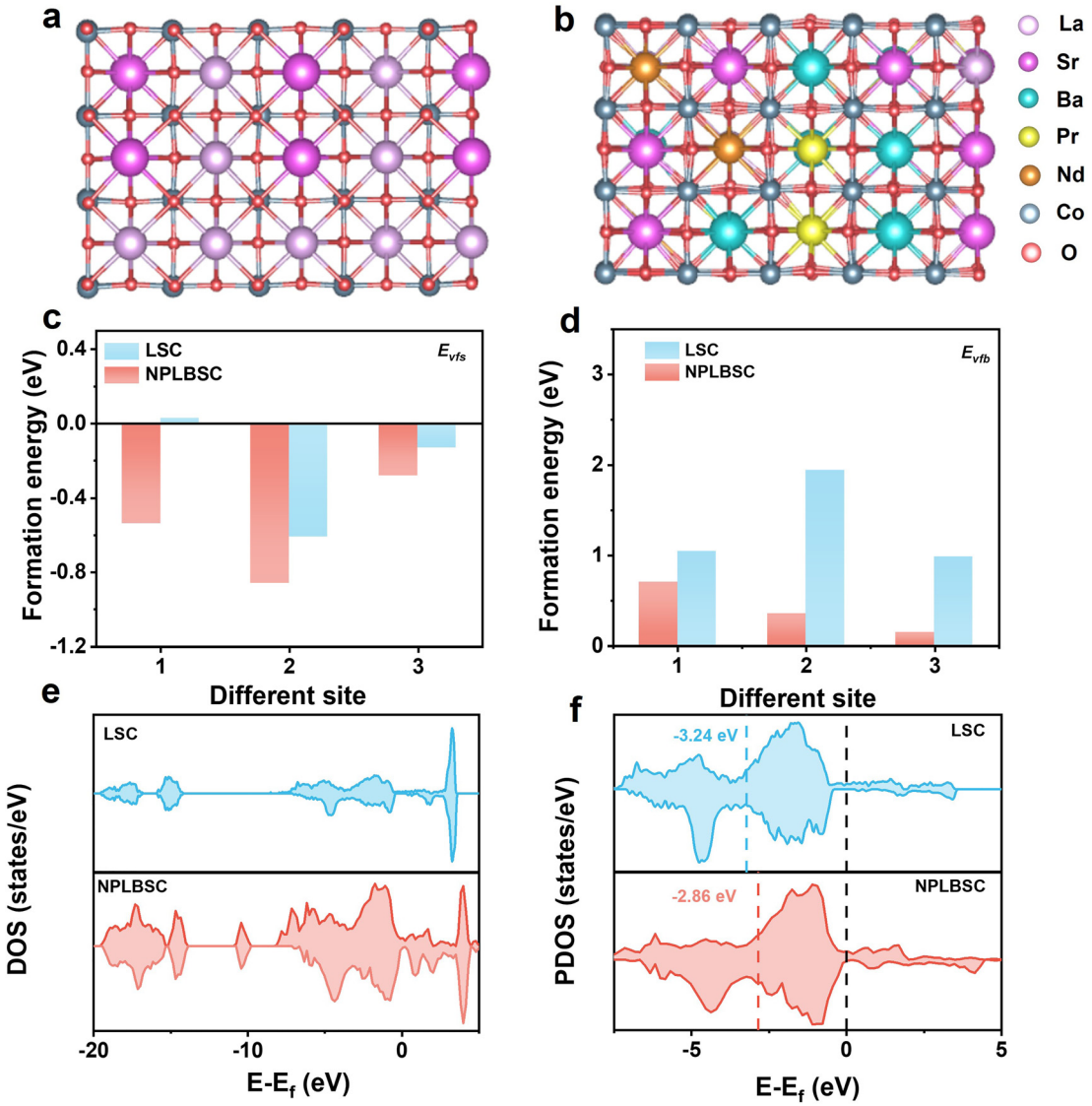

Fig. 5 DFT calculation results. The geometric model of (a) LSC perovskite and (b) NPLBSC with random distribution of A site. Diagrams of formation energy of oxygen vacancy (c) on surface and (d) in bulk of the LSC and NPLBSC. (e) Total density of states and (f) partial density of states of the O 2p-band of LSC and NPLBSC and the corresponding band center relative to the Fermi level.

and NPLBSC. The density of states in Fig. 5e show that NPLBSC possesses much higher states around Fermi level than LSC, indicating that NPLBSC may have higher electronic conductivity.[22] The partial density of states of O 2p as shown in Fig. 5f unveils that the O 2p band center shifts towards the Fermi level from −3.24 eV of LSC to −2.86 eV of NPLBSC, which leads to a lower barrier for oxygen vacancy formation and oxygen ion migration, explaining well the decreased formation energies of oxygen vacancy in NPLBSC.[9,43,44]

2.5 OER performance tests

To elucidate the effect of CoO_6 octahedral distortion on the high-temperature OER activity in SOEC, electrochemical measurements of CO_2 electrolysis were performed at 800 °C. The cell morphology of the anode and the interface between the porous anode and the dense electrolyte are shown in Fig. S19. Electrochemical impedance spectroscopy (EIS) curves (Fig. S20) show that NPLBSC exhibits the lowest R_p. Fig. 6a shows the EIS curves for LSC and NPLBSC at 1.2 V and 800 °C, where the R_p decreases by 16% compared with those of LSC. Distribution of relaxation time (DRT) analysis provides deeper insights into the elementary polarization processes, which are otherwise overlapped and difficult to distinguish in the EIS spectra. As displayed in Fig. 6b, the DRT plots of LSC and NPLBSC anodes are split into three peaks, marked as P1 (high-frequency), P2 (intermediate-frequency), and P3 (low-frequency), respectively, suggesting three elementary electrode processes. P1 is related to the transportation of O^{2-} across the anode/electrolyte interface, P2 represents the electron transfer and oxygen evolution process at the anode, and P3 denotes the adsorption of CO_2 and the dissociation of intermediate carbonate species at the cathode, respectively.[8,9] Obviously, the P1 and P2 areas of NPLBSC anode are smaller than those of LSC, indicating that the NPLBSC anode has faster O^{2-} migration and oxygen evolution rates.

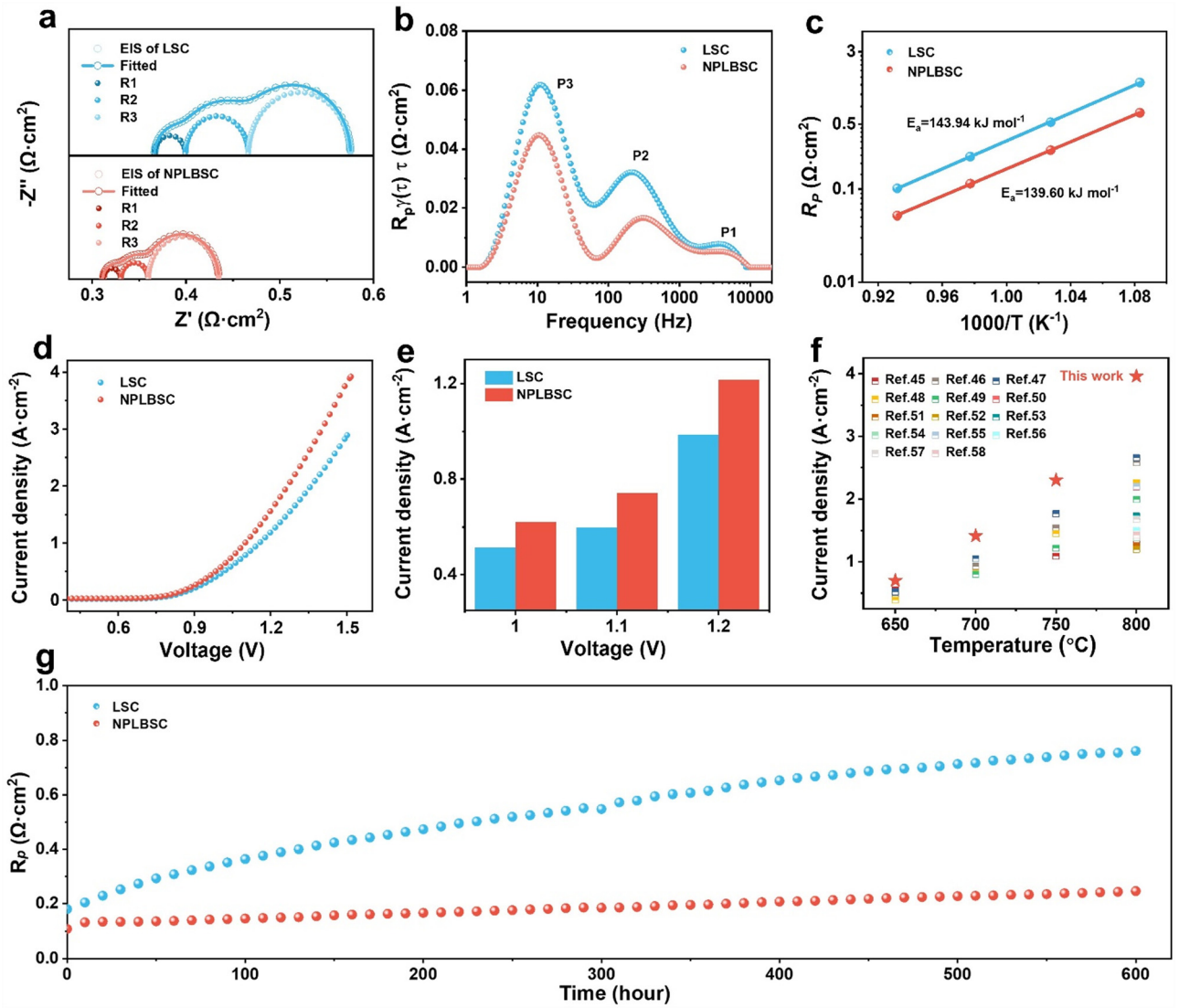

Fig. 6 Electrochemical performances at 800 °C. (a) EIS spectra of the SOECs at 1.2 V. (b) DRT plots. (c) Arrhenius plot of the R_p and activation energy (E_a). (d) Current density–voltage curves (J–V) at 800 °C. (e) Chronoamperometry curves at different voltages. (f) Comparison of the performance for the NPLBSC anode with those of recently reported anodes at 1.5 V. (g) Stability test of R_p in symmetrical cells.

Furthermore, the complex nonlinear least-squares (CNLS) fitting of the EIS spectra was performed according to the DRT analysis results (Fig. S21). With CoO_6 octahedral distortion, the values of R1 and R2 are decreased by 18% and 27%, respectively (Fig. S22). The results show that the performance improvement is mainly ascribed to the accelerated oxygen transport and the surface evolution process, which is in agreement with the ECR results.

Meanwhile, the Arrhenius plots of R_p in Fig. 6c show that the activation energy (E_a) decreases from 143.91 kJ mol^{-1} of LSC to 139.60 kJ mol^{-1} NPLBSC, which further confirms the improved OER activity and faster reaction kinetics of the NPLBSC anode. The improved performance of the NPLBSC anode was further elucidated by the J–V curves (Fig. 6d and Fig. S23). The current density of the NPLBSC anode with thin LSGM (thickness of 160 μm, Fig. S24) can reach 3.96 A cm^{-2} at 1.5 V and 800 °C. The current density of single cell with the NPLBSC anode can reach 0.34, 0.74, and 1.2 A cm^{-2} at 1.0, 1.1, and 1.2 V, respectively, which is higher than that for the LSC anode (Fig. 6e). From the EIS (Fig. S20) and J–V (Fig. S23) curves, we can observe that as the entropy value increases, the R_p gradually decreases, and the current density increases. The superior electrochemical performance of high-entropy perovskite NPLBSC can be attributed to the reduction in the Co–O–Co bond angle (Fig. 2a–d and Fig. S6) and the enhanced distortion of the CoO_6 octahedron (Fig. 2g). This increased distortion results in a higher concentration of oxygen vacancies, which is beneficial for improving the anode OER performance. These findings are further supported by O_2-TPD (Fig. 3g and Fig. S14) and TG (Fig. S15) analyses.

Additionally, the CO production rate and corresponding faradaic efficiency under different applied voltages are shown in Fig. S25. The cell with NPLBSC anode achieved a CO yield of 16.2 mL min^{-1} cm^{-2} at 1.4 V higher than LSC. Meanwhile, the faradaic efficiency of all the anodes approaches to 100% at

different voltages, indicating that the main product is CO without leakage. As reported elsewhere, under similar operating conditions, the electrochemical performance of the NPLBSC anode exceeds most reported anode materials (Fig. 6f).[45–58] Moreover, the stability tests in symmetrical cells (Fig. 6g) show that the NPLBSC anode possesses remarkably slower degradation rate of R_p compared to LSC during the 600-hour durability test, indicating that NPLBSC exhibits great potential as an efficient SOEC anode for the high-temperature OER.

3. Conclusions

In conclusion, we visualized the distortion of oxygen octahedra at the atomic scale and demonstrated its impact on lattice oxygen activity and high-temperature OER performance in SOECs. Specifically, the distortion of CoO_6 octahedra in NPLBSC perovskite activates the lattice oxygen, prompting bulk oxygen mobility and surface reaction activity. Consequently, the NPLBSC anode exhibits higher OER performance than the LSC anode and most reported anode materials, with the current density of 3.96 A cm^{-2} at 1.5 V and 800 °C. This work establishes the relationship between oxygen octahedral distortion in perovskites and catalytic activity for high-temperature oxygen evolution reaction, paving the way for new strategies in the design of SOEC anode materials.

4. Experimental section

4.1 Chemicals and materials

$Nd(NO_3)_3{\cdot}6H_2O$ (Aladdin Industrial Corporation, AR), $Pr(NO_3)_3{\cdot}6H_2O$ (Aladdin Industrial Corporation, AR), $La(NO_3)_3{\cdot}6H_2O$ (Aladdin Industrial Corporation, AR), $Ba(NO_3)_2$ (Sino pharm Chemical Reagent, AR), $Sr(NO_3)_2$ (Aladdin Industrial Corporation, AR), $Co(NO_3)_2{\cdot}6H_2O$ (Aladdin Industrial Corporation, AR), $Fe(NO_3)_3{\cdot}9H_2O$ (Aladdin Industrial Corporation, AR), $Ce(NO_3)_3{\cdot}6H_2O$ (Aladdin Industrial Corporation. AR), $Sm(NO_3)_3{\cdot}6H_2O$ (Aladdin Industrial Corporation, AR), polyvinyl alcohol (PVA), (Sino pharm Chemical Reagent, AR), ammonium citrate (Sinopharm Chemical Reagent, AR), ethylene diamine tetraacetic acid (EDTA) (Sino pharm Chemical Reagent, AR), monohydrate citric acid (CA) (Sino pharm Chemical Reagent, AR), $La_{0.8}Sr_{0.2}Ga_{0.8}Mg_{0.2}O_{3-\delta}$ (LSGM) (fuel cell materials), ethyl cellulose (SECOMA), α-terpineol (Alfa Aesar), ammonium hydroxide (Aladdin Industrial Corporation, AR), 95% CO_2–5% N_2 (Dalian Special Gases), pure CO_2 (Dalian Special Gases), and 5% $^{18}O_2$–95% Ar (Changyou Gas) were used.

4.2 Synthesis of electrode materials

All electrode materials were synthesized using the sol–gel method, with variations of complexing agents. To synthesize anode perovskite powders, the stoichiometric ratios of precursor nitrates were dissolved in deionized water and heated to 80 °C with stirring, and the complexing agents CA and EDTA were added at a molar ratio of total metal ions of 2 : 1 : 1. Subsequently, the pH was adjusted to 8 with ammonium hydroxide, and the solution was heated and stirred at 80 °C until all the water evaporated, resulting in a fluffy black powder. This powder was sintered in a muffle furnace at 1100 °C in air for 5 hours. The $La_{0.6}Sr_{0.4}Co_{0.2}Fe_{0.8}O_{3-\delta}$ (LSCF6428) cathode material was synthesized using the traditional combustion method.[9] Typically, metallic nitrates were dissolved in deionized water and ammonium citrate was added with 1.5 times molar ratio of the metal cations. Then nitric acid was added to adjust the solution pH to 2. The solution was heated and stirred at 80 °C until spontaneous combustion, which was followed by sintering the powder in a muffle furnace at 950 °C in air for 5 hours. For the synthesis of $Sm_{0.2}Ce_{0.8}O_{2-\delta}$ (SDC), metallic nitrates were dissolved in deionized water according to the stoichiometric ratio, and then PVA and CA were added in equal masses, with 125 g of PVA per mole of SDC produced. The solution was heated at 80 °C until a yellowish powder was formed, and then sintered in a muffle furnace at 800 °C in air for 3 hours.

4.3 Cell fabrication

LSGM powder mixed with PVP at a weight ratio of 97 : 3 was dry-pressed at 11 MPa and calcined at 1450 °C for 10 hours in air to obtain an electrolyte with a thickness of ∼560 μm and a diameter of ∼20 mm. An electrolyte disk of about 160 μm in thickness and 16 mm in diameter was prepared by tape casting. The LSCF–SDC cathode slurry was prepared by grinding LSCF (0.3 g), SDC (0.2 g), and solvent mixture (0.3 g, 88% terpineol and 12% ethylcellulose). The anode slurry was made similarly. For the single cell with the electrolyte thickness of ∼560 μm, the cathode slurry was printed on one side of the LSGM with an electrode area of 0.78 cm^2, and the anode slurry on the other side with an electrode area of 0.50 cm^2. For the thin electrolyte (∼160 μm), the anode was printed with a 0.28 cm^2 area, and the cathode was printed with the area of 0.78 cm^2. After printing, the single cell was dried under a heating lamp and then sintered at 1150 °C for 2 hours. Before testing, the gold paste was coated on both sides of the electrode for current collection. The anode slurry was printed onto both sides of the LSGM pellets and then sintered in air at 1150 °C for 2 hours in a muffle furnace to obtain ready-to-use symmetrical cells.

4.4 Materials characterization

X-ray diffraction (XRD, PANalytical X'pert PPR diffractometer using Cu Kα with a wavelength of 1.5418 Å) was used to examine the crystalline structure of the materials at 40 kV and 40 mA. The morphologies of the cell interfaces were meticulously examined utilizing JSM-7900F and JSM-7800F field emission scanning electron microscopes (SEM). JEOL JEM ARM300F atomic-resolution scanning transmission electron microscope (STEM) was employed to acquire high-angle annular dark-field (HAADF) images, annular bright-field (ABF) images along the [110] zone axis of powders, atomic-resolution X-ray energy-dispersive spectroscopy (EDS) maps, and electron energy-loss spectroscopy (EELS) results. X-ray photoelectron spectroscopy (XPS) spectra were obtained using an Al Kα X-ray source and a pass energy of 20 eV on a Thermo Fisher

Escalab 250 Xi to evaluate the material properties. The binding energy positions were calibrated by the C 1s peak at 284.6 eV. The Co–K edge XANES (X-ray absorption near edge structure) and EXAFS (extended X-ray absorption fine structure) spectra were acquired at the BL11B beamline of the Shanghai Synchrotron Radiation Facility (SSRF) and calibrated using pure Co foil absorption edges. Data were processed using Athena software. *In situ* XAS measurements of the SOECs with LSC and NPLBSC anodes were conducted at 800 °C in air. The absorption coefficients were background-subtracted, normalized to energy $\mu(E)$, and reported as "normalized absorption" with respect to E_0 for all the samples. O_2 temperature-programmed desorption (O_2-TPD) and $^{18}O_2$ exchange experiments were conducted using an Auto Chem II 2920 test system. For O_2-TPD, 100 mg of the powder was placed in a U-tube and exposed to synthetic air at 50 mL min^{-1}. The sample was heated to 800 °C for 1 hour and cooled to room temperature. Then He gas was introduced at 50 mL min^{-1} for 50 minutes. Afterward, the O_2 desorption process was carried out at a heating rate of 10 °C min^{-1} with a He flow rate of 50 mL min^{-1}. The evolved gases were analyzed using an online quadrupole mass spectrometer (OmniStar), detecting the m/z = 32 signal. For the $^{18}O_2$ isotope exchange, 100 mg powder was pre-heated to 800 °C in air at 50 mL min^{-1} for one hour which was changed to He at 50 mL min^{-1}. After 30 minutes, the sample was cooled to room temperature. Finally, the sample was heated from 50 °C to 750 °C at 10 °C min^{-1} feeding $^{18}O_2$ at 50 mL min^{-1} while examining signals with m/z = 32, 34, and 36. Thermogravimetric (TG) analysis was performed using a Germany Netzsch STA449F5. The sample was heated in air to 850 °C to remove surface-adsorbed impurities, and then analyzed in N_2 from room temperature to 850 °C at a heating rate of 10 °C min^{-1} with the weight changes recorded. The electrical conductivity relaxation (ECR) tests were conducted using a two-electrode four-terminal technique. LSC and NPLBSC powders were pressed in a rectangular stainless-steel mold to obtain green compacts, and then sintered at 1350 °C for 5 hours, resulting in dense bars. The bar-shaped samples were attached to a homemade device, heated up to 800 °C while passing 200 mL min^{-1} of 20% O_2/Ar gas, held for half an hour at 800 °C, and then switched to 5% O_2/Ar. The electron paramagnetic resonance (EPR) data were obtained using a Bruker, A200 instrument from Germany to further detect the oxygen vacancies. Raman spectra were analyzed at 532 nm of laser excitation using NanoWizard in the 200–1800 cm^{-1} scan range. For the *in situ* Raman spectroscopy experiment, silver wires were connected to a single cell with different anodes. The SiO_2@Au was added to the anode as a surfactant. The anode was exposed to air and heated to 600 °C. Different currents were applied, and spectra were recorded using a LabRAM HR 800 Raman spectrometer equipped with a 532 nm laser and a 50× objective.

4.5 Electrochemical measurements

The electrochemical performance of the SOEC for CO_2 electrolysis was evaluated using a double-electrode four-terminal test system. The anode was exposed to ambient air, while the cathode was fed with 95% CO_2 + 5% N_2 to assess the electrochemical data (J–V, EIS, I–t) using an Autolab (PGSTAT302N, Metrohm, Switzerland). The stability of symmetrical cells was evaluated in air at 800 °C, with resistances measured under open-circuit voltage (OCV). Gas chromatography (Agilent GC8860, equipped with PPU capillary columns and TCD detectors) was performed to detect gas quantification online.

4.6 Computational details

The first principles density functional theoretical calculations are conducted using the Vienna *ab initio* simulation package (VASP).[59,60] The generalized gradient approximation (GGA) of Perdew, Burke, and Ernzerhof is used as the exchange–correlation functional.[61,62] The projected augmented wave potentials are applied to account the valence electrons and ionic core interactions. The DFT+U was applied in order to correct the significant self-interaction error in describing localized d- or f-electrons with strong correlations; an on-site Hubbard term U_{eff} was added to the open-shell d- or f-electrons, 4.0 eV for Co, 6.0 eV for Pr, 6.0 eV for Nd. Plane wavefunctions are expanded to a cutoff energy of 400 eV. Only the gamma point of the Brillouin zone was used for sampling. The convergence threshold was set to 0.05 eV Å^{-1} for geometry optimization. The LSC model is composed of 135 oxygen atoms, 45 Co atoms, 18 Sr atoms, and 27 La atoms, while NPLBSC model is composed of 135 oxygen atoms, 45 Co atoms, 9 Sr atoms, 9 Ba atoms, 9 La atoms, 9 Pr atoms, and 9 Nd atoms, with randomly sites for Sr, Ba, La, Pr, Nd elements by a homemade script.

The high-entropy alloy models with different doping sites is directly compared with the total energy since the elemental counts are identical.

For the calculations of oxygen vacancy formation energy (E_{vf}), E_{vf} was defined as

$$E_{\mathrm{vf}} = \left(E_{\mathrm{vac}} + \frac{1}{2}E_{\mathrm{O_2}}\right) - E_{\mathrm{clean}}$$

where E_{vac} is the total energy of the structure containing oxygen vacancy, $E_{\mathrm{O_2}}$ is the energy of an isolated oxygen molecule, and E_{clean} is the energy of optimized perfect structure.

Conflicts of interest

There are no conflicts to declare.

Data availability

The data that support the findings of this study are available from the corresponding author, Guoxiong Wang (wanggx@dicp.ac.cn), upon reasonable request.

The data supporting this article have been included as part of the supplementary information (SI). Supplementary information is available. See DOI: **https://doi.org/10.1039/d5ee01370d**.

Acknowledgements

The authors gratefully acknowledge financial support from the National Key R&D Program of China (Grant 2021YFA1502400), the National Natural Science Foundation of China (Grants 22272176, 22125205, 22350710789, 22072146, 22002158, 22321002, and 22402198), the Strategic Priority Research Program of the Chinese Academy of Sciences (Grant XDB0600200), the Joint Fund of the Yulin University and the Dalian National Laboratory for Clean Energy (Grant YLU-DNL Fund 2022008), the Liaoning Binhai Laboratory (Grant LBLF-2023-02), the Fundamental Research Funds for the Central Universities (Grant 20720220008), Dalian National Laboratory for Clean Energy (Grant DNL202007), and the Photon Science Center for Carbon Neutrality (JZHKYPT-2021-07). We thank the staff at the BL14W1 beamline of the Shanghai Synchrotron Radiation Facility for the assistance with the EXAFS and XANES measurements. The authors also thank BL10B in NSRL for characterization experiments using synchrotron radiation.

Notes and references

1 A. Hauch, R. Kungas, P. Blennow, A. B. Hansen, J. B. Hansen, B. V. Mathiesen and M. B. Mogensen, *Science*, 2020, **370**, eaba6118.
2 J. F. Cao, Y. X. Ji and Z. P. Shao, *Chem. Soc. Rev.*, 2024, **53**, 450–501.
3 H. Liu, J. Høgh, P. Blennow, X. F. Sun, Y. Zong and M. Chen, *Appl. Energy*, 2024, **361**, 122938.
4 Y. F. Song, X. M. Zhang, K. Xie, G. X. Wang and X. H. Bao, *Adv. Mater.*, 2019, **31**, 1902033.
5 G. Zou, W. C. Feng, Y. F. Song and G. X. Wang, *J. Electrochem.*, 2023, **29**, 2215006.
6 W. Z. Zhang, M. H. Liu, X. Gu, Y. X. Shi, Z. F. Deng and N. S. Cai, *Chem. Rev.*, 2023, **123**, 7119–7192.
7 Y. F. Li, W. Q. Zhang, Y. Zheng, J. Chen, B. Yu, Y. Chen and M. L. Liu, *Chem. Soc. Rev.*, 2017, **46**, 6345–6378.
8 Q. X. Liu, F. R. Shen, G. H. Song, T. D. Liu, W. C. Feng, R. T. Li, X. M. Zhang, M. R. Li, L. H. He, X. Zheng, S. S. Yin, G. Z. Yin, Y. F. Song, G. X. Wang and X. H. Bao, *Angew. Chem., Int. Ed.*, 2023, **62**, e202307057.
9 W. C. Feng, T. F. Liu, R. T. Li, J. W. Li, X. M. Zhang, Q. X. Liu, J. H. Wang, M. R. Li, Q. Fu, Y. F. Song, G. X. Wang and X. H. Bao, *Chem Catal.*, 2023, **3**, 100504.
10 J. Song, Z. H. Tang, X. Y. Wang, Y. D. Wang, H. W. Li, T. Y. Chen and X. F. Ding, *Energy Fuels*, 2023, **37**, 15076–15083.
11 E. Tezel, A. Whitten, G. Yarema, R. Denecke, J. S. McEwen and E. Nikolla, *ACS Catal.*, 2022, **12**, 11456–11471.
12 C. H. Zhao, Y. F. Li, W. Q. Zhang, Y. Zheng, X. M. Lou, B. Yu, J. Chen, Y. Chen, M. L. Liu and J. C. Wang, *Energy Environ. Sci.*, 2020, **13**, 53–85.
13 Y. H. Wang, M. J. Robson, A. Manzotti and F. Ciucci, *Joule*, 2023, **7**, 848–854.
14 Y. H. Wang, J. P. Liu, Y. F. Song, J. Yu, Y. F. Tian, M. J. Robson, J. Wang, Z. Q. Zhang, X. D. Lin, G. D. Zhou, Z. Wang, L. Y. Shen, H. L. Zhao, S. Grasso and F. Ciucci, *Small Methods*, 2023, **7**, 2201138.
15 C. Oses, C. Toher and S. Curtarolo, *Nat. Rev. Mater.*, 2020, **5**, 295–309.
16 S. S. Aamlid, M. Oudah, J. Rottler and A. M. Hallas, *J. Am. Chem. Soc.*, 2023, **145**, 5991–6006.
17 J. T. Ren, L. Chen, H. Y. Wang and Z. Y. Yuan, *Chem. Soc. Rev.*, 2023, **52**, 8319–8373.
18 A. Sarkar, Q. S. Wang, A. Schiele, M. R. Chellali, S. S. Bhattacharya, D. Wang, T. Brezesinski, H. Hahn, L. Velasco and B. Breitung, *Adv. Mater.*, 2019, **31**, 1806236.
19 W. C. Feng, J. C. Yu, Y. L. Yang, Y. G. Guo, G. Zou, X. J. Liu, Z. Chen, K. Dong, Y. F. Song, G. X. Wang and X. H. Bao, *Acta Phys. -Chim. Sin.*, 2023, **40**, 2306013.
20 Z. M. Wang, T. Tan, K. Du, Q. M. Zhang, M. L. Liu and C. H. Yang, *Adv. Mater.*, 2023, **36**, 2312119.
21 Z. Q. Liu, Z. J. Tang, Y. F. Song, G. M. Yang, W. R. Qian, M. T. Yang, Y. L. Zhu, R. Ran, W. Wang, W. Zhou and Z. P. Shao, *Nano-Micro Lett.*, 2022, **14**, 217.
22 F. He, F. Zhu, D. L. Liu, Y. C. Zhou, K. Sasaki, Y. Choi, M. L. Liu and Y. Chen, *Mater. Today*, 2023, **63**, 89–98.
23 F. He, Y. C. Zhou, T. Hu, Y. S. Xu, M. Y. Hou, F. Zhu, D. L. Liu, H. Zhang, K. Xu, M. L. Liu and Y. Chen, *Adv. Mater.*, 2023, **35**, 2209469.
24 Z. C. Shen, M. Qu, J. L. Shi, F. E. Oropeza, V. A. de la Peña O'Shea, G. Gorni, C. M. Tian, J. P. Hofmann, J. Cheng, J. Li and K. H. L. Zhang, *J. Energy Chem.*, 2022, **65**, 637–645.
25 X. Yu, R. Ren, C. Xu, J. Qiao, W. Sun, K. Sun and Z. Wang, *Chem. Eng. J.*, 2025, **503**, 158541.
26 Z. Du, L. Shen, Y. Gong, M. Zhang, J. Zhang, J. Feng, K. Li, K. Świerczek and H. Zhao, *Adv. Funct. Mater.*, 2024, **34**, 2310790.
27 X. H. Zhang, C. L. Pei, X. Chang, S. Chen, R. Liu, Z. J. Zhao, R. T. Mu and J. L. Gong, *J. Am. Chem. Soc.*, 2020, **142**, 11540–11549.
28 N. Orlovskaya, D. Steinmetz, S. Yarmolenko, D. Pai, J. Sankar and J. Goodenough, *Phys. Rev. B: Condens. Matter Mater. Phys.*, 2005, **72**, 014122.
29 X. Xia, W. X. Chang, S. W. Cheng, C. Huang, Y. Hu, W. B. Xu, L. Zhang, B. Jiang, Z. H. Sun, Y. Y. Zhu and X. D. Wang, *ACS Catal.*, 2022, **12**, 7326–7335.
30 C. Su, X. G. Duan, J. Miao, Y. J. Zhong, W. Zhou, S. B. Wang and Z. P. Shao, *ACS Catal.*, 2017, **7**, 388–397.
31 G. X. Chen, Y. Zhao, G. Fu, P. N. Duchesne, L. Gu, Y. P. Zheng, X. F. Weng, M. S. Chen, P. Zhang, C.-W. Pao, J. F. Lee and N. F. Zheng, *Science*, 2014, **344**, 495–499.
32 R. Shukla, A. Kumar, R. Kumar, S. N. Jha and R. S. Dhaka, *J. Phys. Chem. C*, 2021, **125**, 10130–10139.
33 S. K. Pandey, S. Khalid, N. P. Lalla and A. V. Pimpale, *J. Phys.: Condens. Matter*, 2006, **18**, 10617.
34 Y. X. Zeng, Z. Z. Lai, Y. Han, H. Z. Zhang, S. L. Xie and X. H. Lu, *Adv. Mater.*, 2018, **30**, 1802396.
35 Y. G. Guo, S. Wang, R. T. Li, J. C. Yu, X. M. Zhang, M. R. Li, X. S. Zheng, J. F. Zhu, Y. F. Song, G. X. Wang and X. H. Bao, *Joule*, 2024, **8**, 2016–2032.
36 Z. C. Zhuang, Y. H. Li, R. H. Yu, L. X. Xia, J. R. Yang, Z. Q. Lang, J. X. Zhu, J. Z. Huang, J. O. Wang, Y. Wang,

L. D. Fan, J. S. Wu, Y. Zhao, D. S. Wang and Y. D. Li, *Nat. Catal.*, 2022, **5**, 300–310.

37 J. Suntivich, W. T. Hong, Y.-L. Lee, J. M. Rondinelli, W. Yang, J. B. Goodenough, B. Dabrowski, J. W. Freeland and Y. Shao-Horn, *J. Phys. Chem. C*, 2014, **118**, 1856–1863.

38 Y. L. Zhu, H. A. Tahini, Z. W. Hu, Z. G. Chen, W. Zhou, A. C. Komarek, Q. Lin, H. J. Lin, C. T. Chen, Y. J. Zhong, M. T. Fernández-Díaz, S. C. Smith, H. T. Wang, M. L. Liu and Z. P. Shao, *Adv. Mater.*, 2020, **32**, 1905025.

39 D. Q. Guan, G. H. Ryu, Z. W. Hu, J. Zhou, C. L. Dong, Y. C. Huang, K. F. Zhang, Y. J. Zhong, A. C. Komarek, M. Zhu, X. H. Wu, C. W. Pao, C. K. Chang, H. J. Lin, C. T. Chen, W. Zhou and Z. P. Shao, *Nat. Commun.*, 2020, **11**, 3376.

40 J. H. Kim, S. Yoo, R. Murphy, Y. Chen, Y. Ding, K. Pei, B. T. Zhao, G. Kim, Y. Choi and M. L. Liu, *Energy Environ. Sci.*, 2021, **14**, 1506–1516.

41 Y. Chen, S. Yoo, Y. Choi, J. H. Kim, Y. Ding, K. Pei, R. Murphy, Y. X. Zhang, B. T. Zhao, W. L. Zhang, H. J. Chen, Y. Chen, W. Yuan, C. H. Yang and M. L. Liu, *Energy Environ. Sci.*, 2018, **11**, 2458–2466.

42 J. C. Dong, X. G. Zhang, V. Briega-Martos, X. Jin, J. Yang, S. Chen, Z. L. Yang, D. Y. Wu, J. M. Feliu, C. T. Williams, Z. Q. Tian and J. F. Li, *Nat. Energy*, 2019, **4**, 60–67.

43 X. Xi, J. Liu, W. Luo, Y. Fan, J. Zhang, J.-L. Luo and X.-Z. Fu, *Adv. Energy Mater.*, 2021, **11**, 2102845.

44 A. Grimaud, O. Diaz-Morales, B. Han, W. T. Hong, Y.-L. Lee, L. Giordano, K. A. Stoerzinger, M. T. M. Koper and Y. Shao-Horn, *Nat. Chem.*, 2017, **9**, 457–465.

45 C. Y. Lu, C. M. Xu, W. Sun, R. Z. Ren, J. S. Qiao, Z. H. Wang, K. N. Sun, G. Pan and Y. H. Cao, *J. Power Sources*, 2023, **574**, 233134.

46 S. W. Zhang, C. Y. Yang, Y. N. Jiang, P. Li and C. R. Xia, *J. Energy Chem.*, 2023, **77**, 300–309.

47 S. W. Zhang, Y. N. Jiang, H. R. Han, Y. H. Li and C. R. Xia, *ACS Appl. Mater. Interfaces*, 2022, **14**, 28854–28864.

48 L. J. Zhang, Y. N. Jiang, K. Zhu, N. Shi, Z. U. Rehman, R. R. Peng and C. R. Xia, *Small Methods*, 2024, **8**, 2301686.

49 C. Sun, L. Z. Bian, J. Qi, W. Yu, S. T. Li, Y. T. Hou, L. J. Wang, J. Peng and S. L. An, *J. Power Sources*, 2022, **521**, 230984.

50 Y. F. Song, J. Y. Min, Y. G. Guo, R. T. Li, G. Zou, M. R. Li, Y. P. Zang, W. C. Feng, X. Q. Yao, T. F. Liu, X. M. Zhang, J. C. Yu, Q. X. Liu, P. Zhang, R. S. Yu, X. Z. Cao, J. F. Zhu, K. Dong, G. X. Wang and X. H. Bao, *Angew. Chem. Int. Ed.*, 2024, **63**, e202313361.

51 Y. X. Shen, T. F. Liu, R. T. Li, H. F. Lv, N. Ta, X. M. Zhang, Y. F. Song, Q. X. Liu, W. C. Feng, G. X. Wang and X. H. Bao, *Natl. Sci. Rev.*, 2023, **10**, nwad078.

52 H. F. Lv, L. Lin, X. M. Zhang, R. T. Li, Y. F. Song, H. Matsumoto, N. Ta, C. B. Zeng, Q. Fu, G. X. Wang and X. H. Bao, *Nat. Commun.*, 2021, **12**, 5665.

53 L. Y. Lu, D. B. He, R. Fang, C. S. Ni and J. T. S. Irvine, *J. Power Sources*, 2023, **580**, 233424.

54 M. Marasi, L. Duranti, I. Luisetto, E. Fabbri, S. Licoccia and E. Di Bartolomeo, *J. Power Sources*, 2023, **555**, 232399.

55 A. Akhmadjonov, K. T. Bae and K. T. Lee, *Nano-Micro Lett.*, 2024, **16**, 93.

56 D. B. He, W. J. Ruan, J. B. Li, J. P. Ni and C. S. Ni, *Chem. Eng. J.*, 2022, **433**, 133632.

57 J. W. Li, Q. X. Liu, Y. F. Song, H. F. Lv, W. C. Feng, Y. X. Shen, C. Z. Guan, X. M. Zhang and G. X. Wang, *Green Chem. Eng.*, 2022, **3**, 250–258.

58 Y. J. Zhou, T. F. Liu, Y. F. Song, H. F. Lv, Q. X. Liu, N. Ta, X. M. Zhang and G. X. Wang, *Chin. J. Catal.*, 2022, **43**, 1710–1718.

59 G. K. a J. Furthmüller, *Phys. Rev. B: Condens. Matter Mater. Phys.*, 1996, **54**, 11169–11186.

60 G. Kresse and J. Furthmüller, *Comput. Mater. Sci.*, 1996, **6**, 15–50.

61 P. E. Blöchl, *Phys. Rev. B: Condens. Matter Mater. Phys.*, 1994, **50**, 17953–17979.

62 G. K. a D. Joubert, *Phys. Rev. B: Condens. Matter Mater. Phys.*, 1999, **59**, 1758–1775.